Mechanistic modeling of the elution behavior and convective entrapment of vesicular stomatitis virus on an ion exchange chromatography monolith

Adrian Schimek [a] , Judy Ng [a,*] , Federico Will [b] , Jürgen Hubbuch [c,**]

[a] *ViraTherapeutics GmbH, Bundesstraße 27, 6063 Rum, Austria*
[b] *Boehringer Ingelheim Pharma GmbH & Co.KG, Birkendorfer Str. 65, 88397 Biberach, Germany*
[c] *Karlsruhe Institute of Technology, Institute of Process Engineering in Life Sciences, Section IV Biomolecular Separation Engineering, Fritz-Haber-Weg 2, 76131 Karlsruhe, Germany*

ABSTRACT

Developing a downstream purification process for replication-competent enveloped virus particles presents a significant challenge. This is largely due to the highly complex particle structures, as well as complexities of emerging purification modalities for such virus particles. In this study, an unexpected fluid-dynamic effect was observed during the elution of enveloped virus particles from an ion exchange chromatography monolith. This effect led to peak tailing and the separation of virus particle subpopulations. Upon considering possible causes, convective entrapment was identified as a plausible explanation. To investigate this effect, a mechanistic modeling approach representing the electrostatic resin interactions and the convective entrapment effect was implemented. The introduced Langmuir approximation of the convective entrapment showed good alignment with reference data from experiments. The model reproduced the retention effect, and furthermore suggested two virus particle populations due to the stronger retention effect on the tailing subpopulation caused by convective entrapment.

1. Introduction

Viral vector-based therapeutics have advanced significantly in the recent years, enhancing their therapeutic potential, safety, and efficacy [1,2]. This development is reflected in the current clinical landscape, highlighting the demand for suitable bioprocesses for viral vector production [3]. Virus particles (VPs) are large, complex biomolecules with unique structures, sizes, and shapes. These attributes can vary tremendously between different viruses, presenting unique challenges for process development and making it difficult to establish standard platform processes [4,5]. Enveloped viral particles tend to be susceptible to malformation and possibly degradation during bioprocessing. This necessitates the development of mild production processes with short processing times and minimal number of unit operations. A chromatographic capture step can be implemented after the clarification of harvest material, which has typically a high feed volume with low VP concentrations [6]. It is designed to concentrate VPs while reducing working volume using a positive mode (bind-and-elute, BE).

For viral vector chromatography, significant progress has been made in the development of the interacting resin surface as well as resin structure. Affinity chromatography (AC) has demonstrated good performance for some viral vectors [7], though the specificity of AC ligands limit their versatility, and harsh conditions are required for elution [8, 9]. Ion exchange chromatography (IEX), on the other hand, offers greater versatility due to its lower specificity, but it requires more optimization for efficient VP purification [9]. While potential high salt elution conditions of IEX may cause osmotic stress on VPs, they are still milder than those of AC. IEX serves as the primary alternative to AC for the capture step and can also be used for polishing [7].

Large enveloped viral particles present both opportunities and challenges. While they offer a substantial gene insert capacity, their size impedes diffusional movement and obstructs pore accessibility of conventional porous bead-based resins. Convective-driven chromatographic media like monoliths, membranes, and nanofibers offers minimal mass transfer resistances and low pressure drops, facilitating high flow rates ideal for capture steps [10–12]. However, industrial

experience using convective media for enveloped VPs is rather limited, and a deeper understanding of the manifold process challenges for a variety of virus vectors is needed. Monoliths are chromatographic columns comprising a continuous and homogenous structure. Polymer-based monoliths are designed to be made of convective channels, enabling a high mass transfer [13,14]. Silica-based monoliths on the other hand have a bimodal pore size distribution with convective channels and diffusional pores. The latter are inaccessible to large biomolecules, limiting their use in VP purification [15].

Modeling of chromatography purification steps for non-enveloped VP and virus-like particles (VLPs) is performed in recent years to optimize process conditions [16–19] and to gain process understanding [12]. Particularly, mechanistic chromatography models are *in silico* representations to simulate chromatographic process steps. They are based on mathematical equations to represent fluid dynamics as well as physico-chemical phenomena within a chromatographic column. The biopharmaceutical industry leverages the predictive capabilities of mechanistic models to optimize [20], simulate scale-up conditions [21], conduct root-cause investigations [22] and robustness studies [23]. Effort is initially invested to characterize and understand the phenomena within the column to effectively derive accurate mathematical equations to describe it. In the process of developing the model, process knowledge is gained.

Two examples of chromatography modeling for enveloped VPs and VLPs can be found in literature, both involving anion exchange chromatography (AEX) membrane adsorbers. Pamenter et al. observed a time-dependent irreversible sorption of lentiviral vectors, and subsequently developed a kinetic model that can predict recovery losses [24]. Vicente et al. applied the steric mass action (SMA) formalism to describe the resin interaction of Sf9-derived Baculovirus particles and to examine the impact of ligand density on impurity depletion in a gel-layered membrane adsorber [25]. They concluded that the ligands in the gel layer were inaccessible to the large virus particles, unlike the small impurities. However, this feature specific to virus particles was not represented in the model equations. Zhao et al. extended the SMA formalism to exclude ligands within bead pores inaccessible to large virus particles [26]. This extension increased the accuracy of the steric shielding SMA parameter for an enveloped and non-enveloped virus particles in bead-based chromatography systems.

In this study, we used a modified vesicular stomatitis virus (VSV) of the Rhabdoviridae family known as VSV-GP [27], an enveloped virus particle with a bullet-shaped morphology of dimensions of approximately 70 × 200 nm [28]. Production involves propagation in a mammalian cell suspension, and purification by filtration and chromatography steps [29]. Here we characterize the capture step which involves a cationic exchange chromatography (CEX) monolith. During characterization experiments, peak tailing was observed for VSV-GP eluting in a salt gradient. This tailing could not be explained by our current understanding of fluid dynamics and particle-resin interaction in the monolith. An unexpected effect, namely convective entrapment, arose from this investigation.

A convective entrapment effect has been previously described for large biomolecules trapped in constriction sites of a resin [30]. Trilisky et al. observed a flow dependent fluid-dynamic effect that impacted recovery, although dynamic binding capacity of monoliths are flow-independent [31]. Such constriction sites are convectively flown through but narrow down to a size through which large biomolecules cannot pass. Biomolecules are thereby pushed into the constriction sites by advection, thus becoming entrapped. Entrapped particles can then only be released by diffusing back through the opening, and by chance, taking a different flow path through the resin [30,32]. Trilisky et al. demonstrated this effect for monoliths with channel diameter of 2 μm and for non-enveloped human adenovirus serotype 5 of approximately 100 nm in diameter [30]. Pavlin et al. observed this effect in an analytical monolith with a 6 μm channel diameter for an open circular DNA (ocDNA) plasmid isoform [33]. Recovery reduction due to this

effect was seen at flow rates of 0.5 and 1.0 mL/min. However, more compact DNA structures were not affected. In a preparative setup, this recovery reduction for ocDNA was only observed for 2 μm, but not for 6 μm channels by Kralj et al. [34]. Gabor et al. observed plasmid recovery losses due to convective entrapment on analytical monoliths as well as bead-based columns. The authors were unsuccessful in predicting the losses using the radius of gyration for different plasmid isoforms, suggesting an important role of particle geometry for the entrapment effect [35].

The retention effect due to convective entrapment is currently not accounted for in any transport term of conventional chromatographic mechanistic models. To address this gap, we incorporated the Langmuir model to approximate the particle retention by convective entrapment, in addition to the SMA formalism for the electrostatic interactions. Consequently, this study presents a mechanistic model that describes the bind-and-elute behavior of enveloped virus particles in a chromatographic monolith, taking into account the particle retention due to convective entrapment.

2. Theory and model design

A mechanistic chromatography model is an *in silico* representation of a chromatographic step utilizing mathematical equations to simulate the fluid dynamics and molecule adsorption and retention. The applied models are presented in this section, together with the implemented modifications for this study.

2.1. Equilibrium dispersive model

A monolithic structure is considered, with its porosity built up by only convective flow channels. Mass transfer is presumed to be non-limiting [13,31], and potential diffusional accessible pores and thus diffusional limitations are neglected. Therefore, the stationary phase concentration q can be directly coupled to the mobile phase concentration c.

In an axial flow column, mass transport by convection through the column is presumed to be independent of the cross-sectional position. The column geometry is thus reduced to a one-dimensional space. The equilibrium dispersive model (EDM) describes the change of the concentration c in the mobile phase (MP) at a coordinate $x \in [0, L_{Col}]$ and a discrete time point $t \in [0, T]$ as shown in Eq. (1), in which u_0 is the applied flow velocity and ε the column porosity. The EDM is composed of an advection term, a dispersion term, and a term for the mass transfer to the stationary phase (SP) [36].

$$\frac{\partial c}{\partial t}(x,t) = -\frac{u_0(t)}{\varepsilon}\frac{\partial c}{\partial x}(x,t) + D_{ax}\frac{\partial^2 c}{\partial x^2}(x,t) - \frac{1-\varepsilon}{\varepsilon}\frac{\partial q}{\partial t}(x,t) \tag{1}$$

In the EDM, all peak broadening effects are lumped together into the apparent dispersion factor D_{app} [36]. In general, contributing factors for chromatographic peak broadening can include: axial molecular diffusion, eddy dispersion, mass transfer limitations (film mass transfer resistance layer, pore diffusion, boundary layer) and adsorption/desorption kinetics [37]. Since mass transfer is assumed to be non-limiting and binding kinetics are accounted for in the binding isotherm, the apparent dispersion factor D_{app} can be reduced to axial effects and becomes D_{ax}.

The EDM is complemented at the inlet ($x = 0$) and outlet ($x = L_{Col}$) by the Danckwerts' boundary conditions [38].

$$\frac{\partial c}{\partial x}(x = 0, t) = \frac{u(t)}{D_{ax}}\left(c_i(x=0,t) - c_{in,i}(t)\right) \; for \; t > 0 \tag{2}$$

$$\frac{\partial c}{\partial x}(x = L_{Col}, t) = 0 \; for \; t > 0 \tag{3}$$

2.2. Steric mass action isotherm

Brooks and Cramer introduced the SMA isotherm in 1992 [39], which assumes a stoichiometric exchange of ions as principle of molecule-ligand binding. The adsorption of component i on the stationary phase is described by the isotherm equation. A total of N_{comp} components including salt ($i = 0$) is considered. Eq. (4) shows the kinetic form of the SMA isotherm which considers the counter-ion concentration in the mobile phase c_0 and the ionic capacity of the stationary phase Λ [40]. The adsorption behavior is dependent on the component-specific parameters characteristic charge ν_i and steric hindrance factor σ_i. The rate of adsorption and desorption is characterized by the equilibriums parameter $K_{eq} = k_{ads}/k_{des}$ and the kinetic parameter k_{kin}. Reference concentrations ($q_{ref} = 1000 \frac{mol}{m_{SP}^3}$, $c_{ref} = 1000 \frac{mol}{m_{MP}^3}$) were applied to make the units of the equilibriums and kinetic parameter independent from the characteristic charge and thus decouple them. This simplifies parameter estimation and the use of reference values within the same dimension of c_0 and Λ improves numerical stability [41].

diameter, ε is the porosity of the monolith, D is the diffusion coefficient of the biomolecule, and d_p the mean channel diameter of the monolith. In theory, at $Pe = 1$, advection and diffusional rate are balanced. At $Pe \ll 1$, the diffusive transport prevails and particles in constriction sites immediately diffuse out again. At $Pe \gg 1$ the advection prevails and thus particles are convectively entrapped in constriction sites.

2.4. Convective entrapment modeling

In an approach to model the convective entrapment (CE) effect, a second isotherm equation, additive to the SMA isotherm, is introduced. Fig. 1 shows the possible binding modalities for a particle in the mobile phase based on the additive isotherms shown in Eq. (6).

$$\frac{\partial q_i}{\partial t} = \frac{\partial q_i^{SMA}}{\partial t} + \frac{\partial q_i^{CE}}{\partial t} \tag{6}$$

Even though convective entrapment is a fluid dynamic effect rather than a binding modality, it can be interpreted as a binding modality due to the temporary restriction of particles in the resin's constriction sites. Entrapment-and-release is an advection- and diffusion-driven process,

$$\frac{\partial q_i^{SMA}}{\partial t} = \frac{1}{k_{kin,i}} \left(K_{eq,i} \, c_{p,i} \left(\Lambda - \sum_{j=1}^{N_{comp}-1} \left(\nu_j + \sigma_j \right) q_j^{SMA} \right)^{\nu_i} q_{ref}^{-\nu_i} - q_i^{SMA} \left(\frac{c_0}{c_{ref}} \right)^{\nu_i} \right) \quad (i = 1, \ldots, N_{comp} - 1) \tag{4}$$

2.3. Convective entrapment effect

Convective entrapment is a fluid-dynamic effect observed in monoliths which depends on advection and the diffusional rate of affected particles. The Peclet (Pe) number was found to be a prediction parameter for convective entrapment. Pe is a dimensionless number describing the ratio of advection to diffusive transport of a physical quantity. Trilisky et al. derived and simplified an equation to estimate the Pe number for the convective entrapment of large biomolecules in monoliths, Eq. (5) [30].

$$Pe \approx \frac{u_s d_b^2}{\varepsilon D d_p} \tag{5}$$

In which u_s is the superficial flow velocity, d_b is the biomolecule

dependent on the flow velocity, column channel geometries and the particle diffusional rate, therefore also temperature and viscosity dependent. For reasons of simplification, the dependencies were lumped together into an entrapment (k_{trap}) and release ($k_{release}$) parameter. These parameters are thus only valid as long as the cumulated process variables are not changed.

In addition, homogenous and single-particle constriction sites were assumed. With these prerequisites, a simple Langmuir isotherm as shown in Eq. (7) was used to represent the convective entrapment effect. The total amount of constriction sites is considered using q_{max}^{CE} of which the sum of entrapped particles q_j^{CE} are subtracted to calculate the amount of available constriction sites.

$$\frac{\partial q_i^{CE}}{\partial t} = c_i \, k_{trap,i} \left(q_{max}^{CE} - \sum_{j=1}^{N_{comp}-1} q_j^{CE} \right) - q_j^{CE} k_{release,i} \quad (i = 1, \cdots, N_{comp} - 1) \tag{7}$$
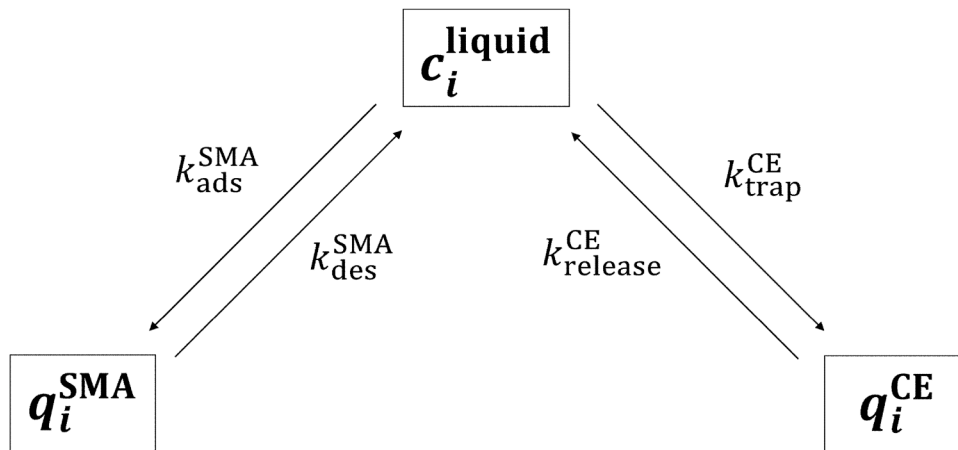

Fig. 1. Isotherm scheme Schematic representation of the isotherm setup. Particles in solution are either entrapped due to convective entrapment or bound to ligands by the SMA formalism.

3. Materials and methods

3.1. Virus preparation

VSV-GP particles were propagated by infection in a mammalian cell suspension. 37 h after infection, the suspension was treated with 200 mM NaCl for viral release. The harvest was clarified by depth filtration, sterile-filtered and treated with nuclease. VPs were captured using a CEX monolith column (CIMmultus SO3, Sartorius BIA Separations, Ajdovščina, Slovenia) and eluted using a 1 M NaCl step at pH 7.5. For polishing and buffer exchange, a preparative size exclusion chromatography column comprising Sepharose 6FF (Cytiva, Marlborough, MA, USA) was used. The mobile phase buffer consisted of a Tris-based buffer with 50 mM NaCl and 150 mM Arginine at pH 7.5. After sterile filtration (0.22 μm), the final virus suspension was aliquoted and stored at -80 °C until usage. The batch was analyzed by qPCR for genomic copies and by TCID$_{50}$ for infectivity resulting in a concentration of 2.3×10^{11} GC/mL and 1.67×10^{10} TCID$_{50}$/mL.

3.2. Chromatographic instrumentation and experimental design

Chromatographic runs were performed on an Äkta micro liquid chromatography (LC) system including an adequate fraction collector (provided by Cytiva, Munich, Germany) unless stated otherwise. PEEK tubing of 0.25 mm inner diameter were used to connect the individual LC system parts except for the column which is mounted on the UV cell. The post-column flow path of the LC system comprised of an UV and a conductivity detector, extended by a multi-angle light scattering (MALS) detector (Wyatt Technology, Santa Barbara, CA, USA).

This study focused on the chromatographic behavior of VSV-GP on a CEX monolith. For this purpose, a scale-down approach was designed. The monolith resin consisted of prototype CIMmic SO3 disks with a manufacturer-specified channel diameter of 6 μm. Three disks were stacked together into the appropriate CIMmic housing, allowing axial flow through all disks with 0.3 mL total volume. The disks and housing were kindly provided by the manufacturer Sartorius BIA Separations (Ajdovščina, Slovenia). Loading densities of virus particles on the monolith resin were kept low (<25 % of max loading capacity) to prevent additional saturation effects. An overview of runs is presented in Table 1.

A Tris-based buffer consisting of 50 mM Tris at pH 7.5 was used throughout this study. The NaCl concentration differed according to the requirements of each step. Column conditioning was conducted using 2 M NaCl for at least 10 column volumes (CVs). 50 mM NaCl were used for column equilibration, loading of virus in BE mode and subsequent wash phase of 5 CV. A linear salt gradient up to 950 mM NaCl was applied for virus particle elution. Different gradient lengths were used as presented in Table 1. In non-binding flowthrough (FT) mode, 500 mM NaCl was used for equilibration and isocratic sample application. After each run, a cleaning-in-place (CIP) step of 2 M NaCl with 1 M NaOH was applied.

3.3. Analytical methods

3.3.1. qPCR titer

The extraction of viral RNA was carried out using the MagMAX Viral RNA isolation kit from Ambion (Life Technologies Corp., Carlsbad, CA, USA), following the instructions provided by the manufacturer. The qPCR analysis was performed using a CFX96 Real Time Cycler from BioRad (Hercules, CA, USA) and the iTaq Universal Probes One-Step Kit, also from Bio-Rad (Hercules, CA, USA). The primers used in the analysis targeted the N-protein gene sequences, as detailed in a previously publication [42].

3.3.2. TCID50 titer

BHK-21 cells (CLS Cell Lines Service GmbH, Eppelheim, Germany) were cultured in 96-well plates using GMEM medium, which was enriched with 10 % fetal calf serum (FCS), 5 % Tryptose Phosphate Broth, and 1 % Penicillin-Streptomycin solution (all media components from Gibco, Thermo Fisher Scientific Inc., Rockford, IL, USA). The cells were then incubated at 37 °C and 5 % CO$_2$. 24 h post-seeding, a series of dilutions of the virus-containing samples were made. The enriched media was used to produce half-log$_{10}$ dilution steps, which were then individually added to the seeded wells. The plates were incubated for a period of 3 days and subsequently the confluence of each well was measured using an automated plate reader (Tecan, Männedorf, Switzerland). A confluence level of ≤ 95 % was set as the threshold to identify cytopathic effects in wells due to infection by infectious particles (IP). The TCID$_{50}$/mL was then calculated based on the number of infected wells using the Spearman-Kärber equation [43,44].

3.3.3. Hydrodynamic radius

The hydrodynamic radius of virus samples was measured by dynamic light scattering (DLS) using a DynaPro Nanostar I (Wyatt Technology, Santa Barbara, CA, USA). Samples were diluted as required using the CEX equilibration buffer described above. The lower fit threshold of the autocorrelation function was adjusted to exclude smaller sample matrix components based on a matrix blank analysis.

3.3.4. HPLC-SEC quantification

For offline quantification of total particle count of virus particles (TP), a method based on a high performance LC (HPLC) device equipped with an analytical size exclusion chromatography (SEC) column was used as described previously [45]. An Acquity Arc Bio HPLC system including a photodiode array (PDA) detector (Waters, Milford, MA, USA) was equipped with the analytical SEC column TSKgel G4000PW (Tosoh Bioscience, Griesheim, Germany). The virus particles were separated from smaller impurities by size and the measured UV signal used for quantification against a calibration curve. The mobile phase consisted of 50 mM Tris–HCl 200 mM NaCl, 150 mM L-Arg, and 0.1 wt-% DMSO, pH 8.0. A constant flow rate of 0.5 mL/min was used. Samples were spiked with bovine serum albumin (BSA) to minimize unspecific adhesion of the VPs to the HPLC vials used.

3.4. Model application and parameter estimation

3.4.1. CADET (Chromatography analysis and design toolkit)

The mechanistic model was build using the CADET open-source framework. CADET is a chromatography-specific modeling and simulation software written in C++ which has built-in functionality for common mass transport and binding models [46]. The CADET source code for the SMA isotherm was modified to implement the convective

Table 1
Overview of chromatographic runs. (FT – Flowthrough; CV – Column volume; BE – Bind and Elute; LGE – Linear gradient elution).

Name	Loading conditions	Run conditions
System characterization	Polystyrene beads (100 nm) 1000 mM NaCl	FT mode; 0.3 mL/min
Low load gradients for Yamamoto method	VSV-GP, <0.1 % of max. loading capacity	BE mode: 20, 40, 60, 80 CV LGE (50 to 950 mM NaCl); 0.3 mL/min
Fraction collection	VSV-GP, approx. 22 % of max. loading capacity	BE mode: 60 CV LGE (50 to 950 mM NaCl); 0.3 mL/min
Reapplication runs	VSV-GP, collected and diluted pools of fraction collection run	BE mode: 60 CV LGE (50 to 950 mM NaCl); 0.3 mL/min
Flow rate variations	VSV-GP, <0.1 % of max. loading capacity	BE mode: 40 CV LGE (50 to 950 mM NaCl) Flow rates: 0.1, 0.25, 0.3, 0.35, 0.45, 0.75 mL/min

entrapment functionality as described in the Section 2.4. In CADET, the implicit differential–algebraic solver (IDAS) time integrator was used to discretize time steps to solve the model's differential-algebraic equation system. In this study, the required Jacobians at every time step were calculated using automatic differentiation. The CADET-Process framework was used to setup the mechanistic model. CADET-Process is an open-source python package with interfaces to external libraries such as CADET to facilitate the setup and parameter estimation of mechanistic models [47].

3.4.2. Yamamoto method

The Yamamoto method is a parameter estimation method based on low load linear gradient elution (LGE) runs to determine SMA isotherm parameters [48]. The method exploits the correlation of salt concentration c_s at the eluting peak maximum of a component with the slope g of the linear gradient applied (Eq. (8)). It thereby calculates K_{eq} and the characteristic charge ν.

$$\log(gV_{solid}) = (\nu + 1)\log(c_s) - \log(\Lambda^\nu K_{eq}(\nu + 1)) \tag{8}$$

3.4.3. Parameter calibration

An inverse parameter estimation method was applied for model parameters for which no other parameter determination method was feasible or available. The inverse method compares simulation data with reference data obtained in experiments and calculates the deviation, in this case, the normalized least square error. This enables the formulation of a minimization problem and allows the application of genetic optimization algorithms such as U-NSGA-III implemented in the pymoo Python package [49]. Within an *a posteriori* specified range, multiple start points were generated. The resulting simulations were evaluated for their error and a new generation of the genetic algorithm was derived.

4. Results and discussion

4.1. System and column characterization

The liquid chromatography system and the chromatography column were characterized for dead volumes and dispersion effects. Detector-specific tracers consisting of a NaCl solution, a dextran solution (blue dextran 2000, Cytiva, Munich, Germany) and a 100 nm polystyrene (PS) bead suspension were used to address different parts of the flow path. The peak maxima of the tracer runs were used to calculate system dead volumes. Column porosity was determined using the net retention time of NaCl and dextran in the column. The porosity determined using NaCl was 3.5 % higher than that derived from the dextran peaks. A mercury intrusion porosimetry analysis was conducted by ZetA Partikelanalytik (Mainz, Germany): the pore volume for pore sizes below 100 nm was approx. 1 % of the total determined pore volume. Based on both findings, the differences in porosities for different molecule sizes (NaCl, dextran and VPs) were regarded negligible and the porosity derived from dextran was used for the model. Dead volumes of 52 μL were considered as ideal plug flow reactors (PFRs) and dispersion was represented using ideal continuous stirred tank reactors (CSTRs) of in total 43 μL. The dispersion contribution of the tubings was expected to be minor. Hence, flow delays of tubings were modeled as ideal PFRs while residual dispersion effects were lumped together with back mixing effects of detector flow cells and other dead volumes as ideal CSTRs. This approach simplified the model setup and calibration. The tubular reactor with an axial dispersion of zero as ideal PFR, and the CSTR unit operation, both included in the CADET-Process package were utilized. The column axial dispersion value was determined by parameter fitting of the NaCl solution runs. Resulting simulations of the characterization runs are displayed in Fig. 2.

To determine ionic capacity, an acid-base-titration was conducted [50]. First, all counter-ions were displaced by protons using 0.5 M HCl.
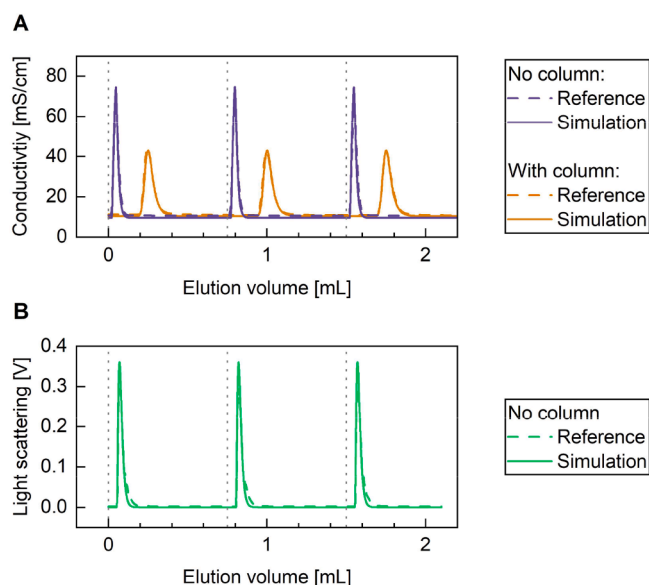

Fig. 2. System and column characterization tracer runs for system and column characterization using (A) NaCl for the conductivity detector and (B) 100 nm PS latex beads for the LS detector. Dashed lines are experimental reference data which are matched by the solid simulation data. Dotted vertical lines mark the injection times of the tracers.

Table 2
Column parameters for the CIMmic SO3 0.3 mL disk stack. Column geometry values are provided by the manufacturer.

Parameter	Symbol	Value	Unit
Column length	L_{Col}	6.3	mm
Column diameter	d_{Col}	7.9	mm
Column volume	V_{Col}	0.3	mL
Axial dispersion	D_{ax}	0.003	mm^2/s
Porosity	ε	0.636	–
Ionic capacity	Λ	0.184	mol/L

Then, a column wash was caried out using purified water. Finally, a titration using 5 mM NaOH was performed until breakthrough was observed in the conductivity signal. The applied amount of sodium ions n_{Na^+} was then used to determine the ionic capacity with Eq. (9). Variables and results are shown in Table 2.

$$\Lambda = \frac{n_{Na^+}}{V_{Col}(1 - \varepsilon)} \tag{9}$$

4.2. SMA parameter estimation

SMA parameters were determined by correlating the salt concentration at peak maxima with the normalized salt gradient slope using four elution gradient lengths (20, 40, 60 and 80 CV) according to Yamamoto et al. [51]. The slope and x-intercept of the regression were used to calculate $\nu = 1000.0$ and $K_{eq} = 12.0$ according to Eq. (8). The results are shown in Fig. 3A.

The determined ν and K_{eq} were used to simulate the low load gradient runs, resulting in a good alignment of the retention times for the peak maxima as shown in Fig. 3B. Fitting of $k_{kin} = 5 \times 10^6$ s enabled the representation of the peak fronts. Additional to the main peaks where the peak maxima were used, all elution chromatograms show a strong tailing which is not represented in the simulation. The SMA approach and the assumption of a homogeneous virus particle population did not account for the observed tailing effects. Since no pore diffusion is present in the model an unaddressed phenomenon must be the cause.
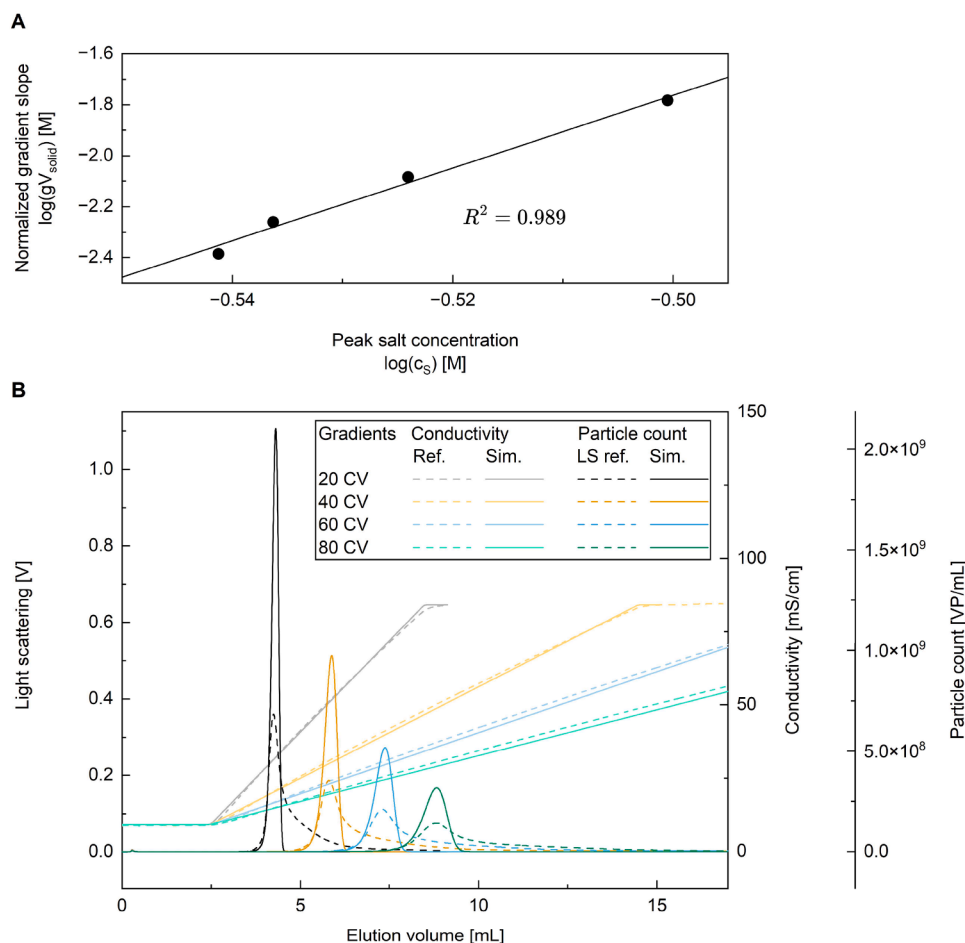
Fig. 3. SMA parameter determination and simulations of low load gradient runs. (A) SMA parameter determination based on the Yamamoto method. Log-log plot of gradient slope and salt concentration at elution maximum yielding in K_{eq} and ν using given equation. (B) Yamamoto LGE runs, conducted at 20, 40, 60 and 80 CV gradient lengths and low loading densities. Experimental reference data and simulations which are based on the SMA parameter determined in A and a fitted kinetic parameter.

4.3. Causes for peak tailing

A variety of factors can contribute to tailing in an elution peak for IEX chromatography: Mass transfer limitations, (extra-column) dispersion effects, sample heterogeneity and secondary particle-resin interactions [37]. These potential causes were considered, using both experimental and theoretical approaches. The findings are presented in this section, and potential contributing factors are discussed.

4.3.1. Peak height and tailing are flow rate dependent

To investigate potential influences from fluid dynamics, the bind-

and-elute run using a 40 CV NaCl-gradient (Fig. 3) was repeated at various flow rates. In the tested range of flow rates between 0.1 to 0.75 mL/min, the elution peak showed changes in the extent of peak tailing as well as peak height depending on the flow rate as shown in Fig. 4. For the previously used flow rate of 0.3 mL/min, the tailing is most pronounced (Fig. 4B, blue line). Deviations of 0.05 mL/min in either direction reduced the tailing. A minimal tailing in the set is reached for the highest flow rate deviations in both direction (Fig. 4A+C) for which the increased flow rates also show a reduced peak height (Fig. 4C). Due to these findings, the influence of flow rate on dispersion was evaluated as presented in the following section.
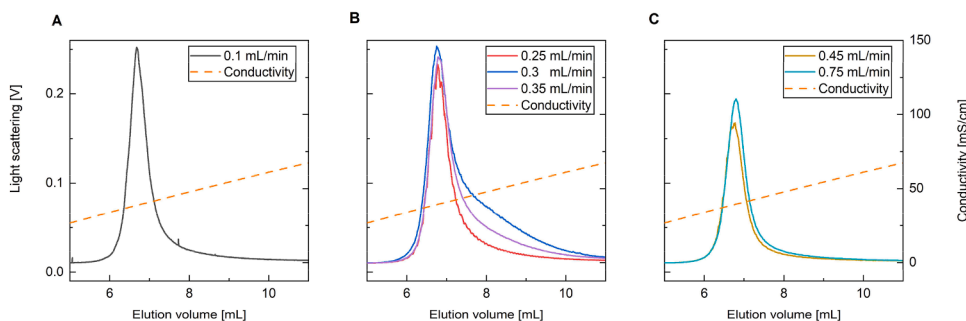

Fig. 4. The impact of flow rate on the elution profile was analyzed by deviating the flow rate between 0.1 and 0.75 mL/min for 40 CVs LGE runs at low loading densities. (A) 0.1 mL/min, (B) (0.3 ± 0.05) mL/min and (C) 0.45 mL/min, 0.75 mL/min.

4.3.2. Possible dispersion effects

Dispersion effects in the column and LC system were characterized and considered as shown in Fig. 2. Furthermore, the influence of flow rate and thus potential impact on the chromatogram was investigated. Acetone pulses were applied on the column at different flow rates. Overlying peaks are observed for higher flow rates between 0.5 to 1.0 mL/min while slightly broader peaks are observed for lower flow rates between 0.1 to 0.25 mL/min (supplemental Figure S1).

From a theoretical point of view, dispersion effects in chromatography can be categorized as either column-originated or extra-column effects. Within the column, the hydrodynamic dispersion due to the resin geometry is a constant parameter according to van Deemter and is independent of the flow rate [52]. The longitudinal (axial) molecular diffusion is dominant for very low flow rates, which is seen using the acetone pulses at very low flow rates in Figure S1 [52]. However, with lower residence times at elevated flow rates and low inherent diffusional rates of large biomolecules, its influence is considered negligible. Thus, it is unlikely that flow rate-induced dispersion effects is responsible for the observed tailing variations in Fig. 4.

For monoliths in disk formats used in this study, observed dispersion is dominated by extra-column effects [14] such as system dead volumes. Tubings, column housing and detector flow cells contribute to the dead volume which becomes more important when using low volumetric columns [53]. In a similar chromatographic setup, Yamamoto et al. observed a fronting and slight tailing which was assumed to originate from dispersion in the column housing [54]. In comparison, tailing effects observed in the results presented here are much more dominant. The setup used for this study was optimized for minimal dispersion effects: the chromatographic system used features small internal volumes, and the axial flow CIM disks exhibit lower dispersion compared to the radial flow monoliths [13]. In the presented study, no relevant peak broadening influence of the flow rate was determined. Observed dispersion effects were constant within the tested flow rate and accounted for in Fig. 2.

4.3.3. Fractions of main peak and tailing show distinct elution behavior

To examine the behavior of virus particles in the main and tailing part of the elution peak separately, the elution peak was fractionated accordingly. The column was loaded to approximately 22 % of its capacity with purified virus particles, and then a 60 CV NaCl-elution gradient at 0.3 mL/min was performed. With this higher loading density, the elution profile (Fig. 5A) remains the same as for the low load runs (Fig. 3B), comprising a main peak and a strong tailing.

Fractions collected throughout the run were quantified by offline HPLC-SEC analysis. The overlay of the light scattering signal at 90° and the offline quantification matches except for the peak maxima where the scatter signal was saturated even though the laser power was reduced to 10 %. The ratio of offline measured VP concentration to the scatter signal of this run was used as measurement factor for this study. The measurement factor of $1.9 \times 10^9 \frac{VP}{mL}/$ V was applied in all plots to visualize the scatter signal of experiments, the reference data, together with simulated virus particle count data at a constant ratio between them.

The fractions at the peak maximum and the mid part of the tailing (indicated in Fig. 5A) were pooled and conditioned (diluted) to adjust the NaCl concentration to the initial binding conditions. The pools were individually reapplied on the regenerated column using the same conditions as for the initial fraction collection run. Reapplication of the two pools resulted in completely different behaviors compared to the initial application and also between the two pools (Fig. 5B). Specifically, the main pool elutes as a sharp peak with minor tailing at the same retention
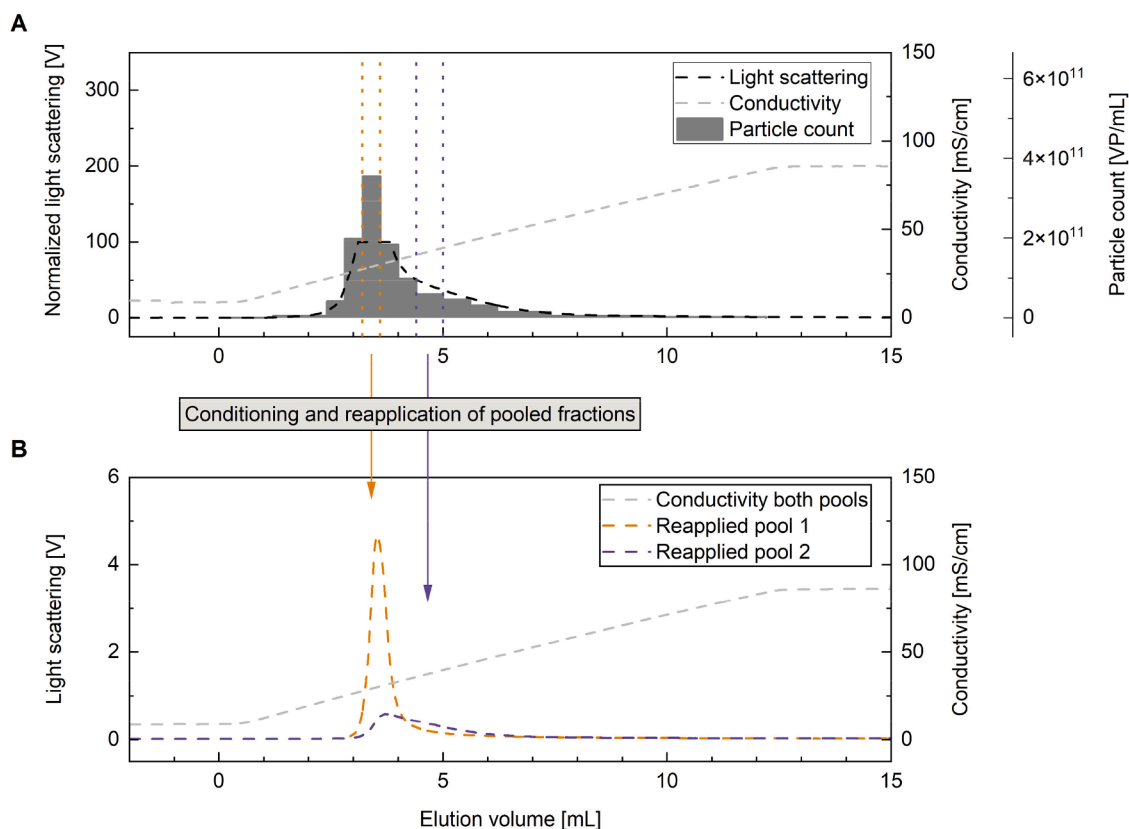

Fig. 5. Main peak and tailing fraction collection and reapplication. (A) Fraction collection of a 60 CVs LGE run with purified VSV-GP. Laser power was reduced to 10 % to prevent saturation which still occurred at peak maxima. The scatter signal shown was normalized to 100 % laser power for comparability. Fractions were colllected and VPs quantified offline by HPLC-SEC. (B) Pools of the main and tailing peak region (marked in A) were reapplied onto the same column using the same bind-and-elute parameters as in A. NaCl concentrations of the pool loads were adjusted by dilution to meet initial sample loading conditions of A.

time as the pool collection. On the contrary, the reapplied tailing pool starts eluting with a small delay compared to the main peak and exhibits a dominant tailing. In this case, however, no distinct peaks can be discriminated. This phenomenon of different elution behaviors of collected fractions was observed also in a scaled-up setup using the same run conditions: 1 mL CIMmultus SO3 column (Sartorius BIA Separations, Ajdovščina, Slovenia) on an Äkta avant150 (Cytiva, Munich, Germany) at 1 CV/min. A different batch of purified virus particles was used which was produced in the same way as the virus material applied to the original experiment. The scaled column uses a radial flow pattern instead of an axial flow in the scale-down approach. Even in this scaled setup and changed flow pattern, the same distinctive elution behavior of virus particles in the main and tailing peak part were observed (Figure S2). In the next sections possible causes which could explain observed effects are discussed.

4.3.4. Charged subspecies and kinetic effects

When multiple peaks or shoulders are observed in an IEX elution gradient, the first logical assumption is that there is a diverse population of subspecies or impurities with different charges. Effio et al. showcased an example where a single target component had to be separated from a complex feed stock. [17] In their highly complex LGE chromatogram, many overlapping peaks are observed which could be deconvoluted into individual components. In their derived model, all components were modeled individually with different and independent SMA parameters [17]. In contrast, the chromatograms observed in this study show a different behavior: no individual distinct peaks are revealed in any of the utilized gradients (Fig. 3B). Instead, a flow rate dependency for the tailing was observed in Fig. 4. The strongest effects were seen at the flow rate of 1 CV/min = 0.3 mL/min. Deviations in both directions decreased the tailing. These observations strongly oppose the tailing effect being originated from charged species.

Another influence on the chromatogram are time-dependent kinetics of the particle-resin-interaction. These effects are amplified in bead-based chromatographic resins due to mass transfer resistances which are considered negligible in this study setup using a monolith. By increasing the kinetic parameter in the kinetic form of the SMA equation, the actual kinetics decrease due its reciprocal form. This results in slowed desorption of components and peak tailing [55]. Decreased kinetics also impact the adsorption term in the SMA equation, leading to a slowed adsorption until breakthrough during loading occurs. The kinetic parameter was fitted to be aligned with the front of the LGE peaks. A further increase of the parameter in the model lead to an early breakthrough of components during the loading phase (data not shown) which is not seen in the reference data set. Slow kinetics were thus excluded as a tailing cause.

4.3.5. Hydrophobic interaction chromatography (HIC) effects

Residual hydrophobic interactions of the polymethacrylate backbone of the monolithic resin may slow down the desorption process of bound particles, especially with salt ions being present. The salting out effect should increase potential hydrophobic interactions, thus a steeper salt gradient for elution should increase effects as observed by Altern et al. for mixed-mode columns [56]. This is not observed in Fig. 3. Moreover, a potential HIC effect would not exhibit a flow rate dependency as observed for the tailing in Fig. 4.

4.3.6. Binding modalities

The shape of VSV particles resembles a bullet with its cylindrical structure, with one flat end and the other one convex. Thus, different binding strengths of the particle facets to the resin surface could be assumed. If so, a certain proportion of the different binding modalities is expected to be established. This proportion would then be observed as the ratio of the peak areas eluting from the column. And the ratio should be re-established when any elution peak fractions are reapplied on the column. Fractions of the main peak and the tailing were collected and

reapplied on the same column using the same process conditions at two different scales (Fig. 5 and Figure S2). Upon reapplication of the pools, the resulting chromatograms show a very different ratio of the main and tailing part. This observation indicates that different binding modalities are most likely not the main contributor to the observed tailing.

4.3.7. On-column particle alterations

Morphological differences in VSV-GP particles were previously described to occur in the preparative process [57] and enveloped virus particles are typically sensitive to environmental stress such as high ionic strength [58] and shear rates [59]. Possible morphological on-column alterations could result in a variety of elution behaviors, thus the broad tailing peak. The reapplication of the main peak does not support this hypothesis. The tailing upon reapplication is reduced to a minimum (Fig. 5B), so no on-column alterations result in an extended tailing behavior. Furthermore, no significant difference in infectivity was determined between the pooled fractions: ratio$_{IP/TP}$ (Main peak) = $14 \pm 7\%$ TCID$_{50}$/VP; ratio$_{IP/TP}$ (Tailing) = $20 \pm 12\%$ TCID$_{50}$/VP.

4.3.8. Convective entrapment

The observed peak tailing may be caused by fluid-dynamic effects rather than particle-resin-interactions. The convective entrapment effect as described by Trilisky et al. [30,32] and Koku et al. [60] is a fluid-dynamic effect leading to partial or complete particle retention. Particles are entrapped in narrowed channels by convective pressure and released by chance due to diffusional movement. This leads to a retention effect observed as a peak delay, tailing effect or peak area reduction.

Convective entrapment can be classified by the Peclet number (*Pe*), a dimensionless number dependent on process parameters such as the flow rate but also on particle characteristics such as the diffusional rate. The Peclet number is used as a predictor for recovery losses due to the convective entrapment effect (*Pe* ≫ 1), but convective entrapment was also observed for *Pe* < 1 [30,33]. In the bind-and-elute runs presented here, the determined Peclet numbers of the utilized flow rate range were *Pe* < 1 (Figure S3). Peclet numbers were estimated based on diffusional rate measurements of VPs using DLS. At the flow rate of 0.3 mL/min for which the strongest tailing effect was observed (Fig. 4B), a $Pe_{0.3} \approx 0.14$ was estimated. At lower flow rates (Fig. 4A), Peclet numbers are lower ($Pe_{0.1} \approx 0.04$) and diffusional transport becomes more dominant: particles would have a higher chance of a fast release from constriction sites by diffusion. Conversely, at higher flow rates the advection compared to diffusional transport becomes dominant, and particles in constriction sites remain entrapped until the conditions change. This leads to a reduced peak height as observed in Fig. 4C. However, this is not represented in the estimated Peclet numbers which are *Pe* < 1 ($Pe_{0.45} \approx 0.2$, $Pe_{0.75} \approx 0.34$) and demonstrates the estimative character of the Peclet number. The correct interpretation of Peclet numbers in the dimension of 1 is difficult due to the equilibrium of advection and diffusional rate. It thus remains unclear at which Peclet value tailing effects due to convective entrapment are most prominent.

The reapplication runs using the main and tailing fractions in Fig. 5 and Figure S2 indicate the presence of at least two populations in the feed material. These are weakly separated due to their different behaviors in terms of the convective entrapment effect. Since the salt-gradient alone cannot effectively separate these populations, it is presumed that there is a morphological difference between them. Particle analysis of the two pools by DLS reveals a difference in the hydrodynamic diameter by 14 nm, with pool 1 measuring 156 nm and pool 2 measuring 170 nm. Based on these findings, we conclude that there are at least two distinct populations within the feed material exhibiting different convective entrapment behaviors. We further suspect that the convective entrapment is likely highly sensitive to even minor differences, which may originate from upstream production conditions and/or alterations from downstream processing. Heterogeneity in functional

and structural properties of VSV particles can arise from the timepoint of budding from the infected host cell [61]. Morphological changes may be further introduced throughout the preparative process due to environmental stress on particles [57]. Differences in VSV particles were observed in this study, however the root cause analysis for the variations is out of scope. It remains unclear if particle heterogeneity originate from the cell culture or is later introduced, eg. during clarification. Particles alterations occurring in the CEX column were excluded as discussed in Section 4.3.7.

Additional runs in non-binding conditions at elevated salt concentrations ($c_{NaCl} = 950$ mM) were conducted. These runs used an initial flow rate of 0.75 mL/min. Subsequently the flow rate was either paused (Figure S4A) or stepwise reduced (Figure S4B). After the initial flow-through peaks, subsequent 'eluting' peaks were detected every time the flow rate conditions changed. 7.5 % of the total peak area was measured after the flow rate pauses while 2.5 % was seen with flow rate reduction. When conducting blank runs without virus particle application or without a column, no subsequent peaks were observed upon flow rate changes (data not shown). Low flow rates are impractical in preparative applications as monoliths are specifically chosen to be used at high flow rates, eg. for high volumetric feeds in initial capture steps. A flow rate reduction after preparative runs can help to evaluate recovery losses due to entrapment effects. Furthermore, CIP steps might be improved by flow rate adjustments to increase the diffusional movement out of constriction sites.

Koku et al. showed a near complete entrapment of Adenovirus particles at high Peclet numbers [60]. In the study presented here, no complete entrapment was observed. Instead, a strong tailing effect was attributed to the entrapment effect already at Peclet numbers below 1. In this range, the impact on recovery might be low, nevertheless for analytical applications it could be important. Loading densities are usually low to start with and retained particles might lead to misinterpreted chromatograms.

4.4. Modeling of convective entrapment effect

Particle retention due to convective entrapment was implemented additionally to the SMA isotherm through an approximation by a Langmuir term. Model parameter estimation and calibration, as well as model insufficiencies due to simplifications are presented.

To estimate the amount of constriction sites of the monolith resin, a pore size distribution analysis was performed. The mercury intrusion porosimetry analysis shown in Figure S5 shows a generally narrow pore size distribution. A pore volume of $V_{Pore} = 1255.0$ mm³/g and a modal pore diameter of 5.47 μm was determined in the analyzed pore size range between 10 nm and 100 μm. The pore volume of pore sizes between 10 nm and 100 nm was considered ($V_{CE} = 12.55$ mm³ /g) for an estimation of the convective entrapment constriction site capacity. A cylindrical approximation using the particle geometry of 70 nm x 200 nm [28] was utilized to determine the single virus particle volume and derive a theoretical maximum number of virus particles fitting in the convective entrapment capacity. The density of the dried monolith resin was determined to be $\rho = 0.491$ g/mL (mean of 4). Using these values, a theoretical convective entrapment capacity of $q_{max}^{CE}(VSV) = 8.01 \times 10^{12}$ particles/mL was calculated. This estimated capacity exceeds the amount of virus particles applied in a single run of this study by a factor of at least 10. The pore size population considered represents only the end volume of presumed funnel-shaped constriction sites whereas virus particles would most likely be stuck above in more spacious geometries. The result is thus a low estimate which still exceeds the number of viral particles applied.

Based on the findings described in Section 4.3, two virus particle populations were assumed. The same SMA parameters, previously determined, were used for both populations which means that the same electro-chemical interaction with the resin is presumed. The convective

Table 3
Resulting parameters from model calibration of the two particle populations.

Parameter	Symbol and unit	Population 1	Population 2
Population share	[−]	0.65	0.35
SMA specific parameters			
Equilibriums constant	K_{eq} [−]	1.0×10^3	1.0×10^3
Kinetic	k_{kin} [s]	5.0×10^{-6}	5.0×10^{-6}
Characteristic charge	ν [−]	12.0	12.0
Steric factor	σ [−]	1.0×10^6	1.0×10^6
CE specific parameters			
Entrapment factor	k_{trap} [m$_{MP}^3$/mol s]	2.150×10^4	2.168×10^5
Release factor	$k_{release}$ [1/s]	3.587×10^{-2}	1.613×10^{-1}

entrapment parameters k_{trap} and $k_{release}$ were calibrated together with the ratio of populations by parameter estimation based on the low load gradient runs. Table 3 summarizes the determined population specific parameters. The difference in the determined convective entrapment parameters reflects their different convective entrapment behavior.

4.5. Predicted chromatograms

The predicted gradient runs using the combined isotherm, Eq. (6), are shown in Fig. 6A. The simulations exhibit a strong peak tailing for all gradient slopes which represents the tailing of the reference data. Individual population signals are shown in Fig. 6B for the 40 CV gradient run: the second population is mainly responsible for the tailing though the first population slightly tails as well. The start of elution for the second population is delayed by approx. 60 s, which can be explained by the retention effect due to convective entrapment after eluting at the same time as the first population. For the steeper gradients, the simulated tailing is observed as a distinct shoulder which differs from the rapidly decreasing tailing in the reference data. The elution of population 2 is simulated as strongly retained which is not the case in the reference data.

The predicted simulations of the fraction collection and reapplication of collected pools are shown in Fig. 7. The simulations of the fraction collection are well aligned to the reference data (Fig. 7A). Based on the simulation, a virtual pooling of eluted material was conducted at the marked volume points. The concentrations of both populations (P1, P2) were determined and the purity in the collected fractions derived by Eq. (10): $purity_{P1}$(Main peak) = 0.89, $purity_{P2}$(Tailing) = 0.69.

$$purity_{Pi} = c_{Pi}/(c_{P1} + c_{P2}), \quad i \in (1, 2) \tag{10}$$

The results were used as feed properties for the subsequent simulations of the reapplied runs (Fig. 7B). The dilution factors to reduce the salt concentration and re-establish initial feed conditions were considered. The consecutive simulations show a good representation of the reference data, even though the tailing of pool 1 is overrepresented compared to the reference.

4.6. Model simplifications

The entrapment model based on the Langmuir-approximation and the presumption of 2 populations distinguished by different entrapment behavior is a simplified approach. There are likely some unaccounted properties or entrapment effects leading to the observed deviations from the reference data and are discussed in the following.

A steep gradient leads to a fast desorption of particles and a locally high concentration of particles in the mobile phase. These concentration differences between the gradients could induce a changed entrapment behavior, especially for population 2, which is not considered in the model. The contrary is observed for the fraction collection run (Fig. 7). The loading density is much higher compared to the LGE runs (approx. 1400-fold) and thus the number of particles desorbing at the same time. Nevertheless, no concentration related fast elution of population 2 is observed. The separation from population 2 is sufficient enough to
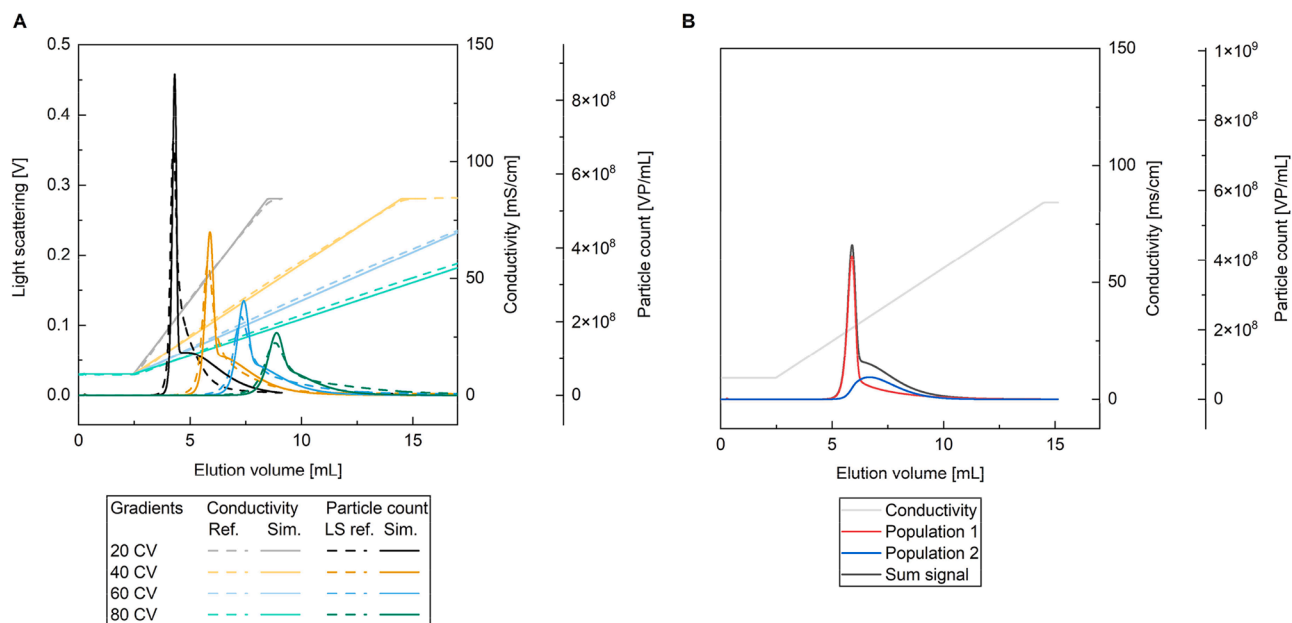
Fig. 6. CE + SMA isotherm simulations of low load gradient elution runs. (A) Simulations of Yamamoto LGE runs, conducted at 20, 40, 60 and 80 CV gradient lengths and low loading densities. Simulations use the combined isotherm (SMA + CE) and two assumed populations. (B) Deconvoluted view of the 40 CVs Yamamoto LGE run displayed in A, showing the individual population signals.
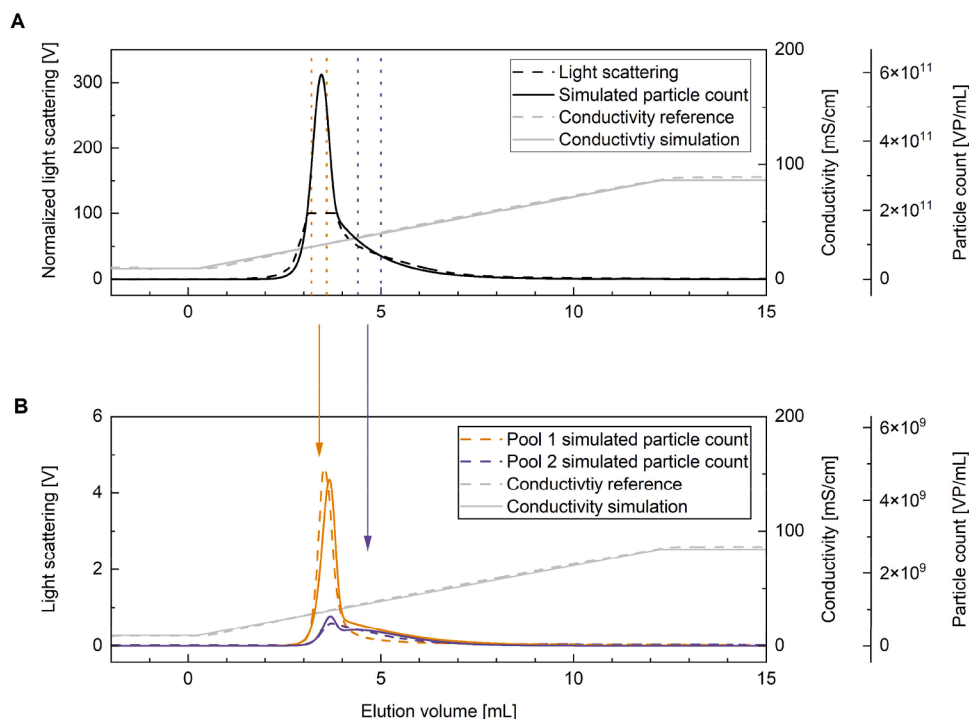

Fig. 7. CE + SMA isotherm simulation of fraction collection and reapplication run. (A) Simulation and experimental reference data of the fraction collection run shown in Fig. 5. Marked fractions were used for pooling of main and tailing peak regions. (B) Simulation and experimental reference data of reapplied pools. Virtual pooling of marked fractions in A yielded in feed properties for the subsequent simulation of reapplication. Simulations in A and B use the combined isotherm (SMA + CE) and two assumed populations.

reduce the tailing of the reapplied pool 1 drastically.

Further simplifications originated from the use of the Langmuir approximation for the convective entrapment effect might result in additional errors. The classic Langmuir model has three preconditions: monolayer adsorption, no particle-particle interaction and homogenous binding sites. Applied to the convective entrapment effect, these preconditions are transformed to: Single particle convective entrapment per

constriction site and homogenous constriction sites. Constriction sites are convective channels which taper off to a narrow passage blocking particles from passing through. This funnel-shaped structure depends on the polymerization conditions and cannot be evaluated in detail. Looking at the structure of polymethacrylate monoliths in scanning electron microscopy (SEM) pictures [62], homogeneous constriction sites cannot be assumed. In regard to multiple particle entrapment in one

constriction site, Trilisky et al. presumed a low probability [30]. They argued that an entrapped particle would reduce the convective flow and reduce the characteristic distance for diffusive release, thus reducing the likelihood of other particles being entrapped after the initial one.

Lastly, the additive setup of SMA and convective entrapment equations in the isotherm considers both effects distinctly without interdependencies. Therefore, particle-ligand-interaction is not considered for particles being entrapped in the constriction sites. However, ligands within constrictions sites can contribute to the binding of particles. Considering the limitation in suitable analytical methods, it is not feasible to determine if the misalignment observed in the simulation compared to reference data is due to insufficient characterization of the feed material or lack of representation of the model of the actual effects.

5. Conclusion

Downstream process development of enveloped virus particles is complex due to the structure of the virus particles and new technologies. This can lead to unforeseen effects that are not well understood. Mechanistic modeling can help identify knowledge gaps and improve our understanding of the process.

In this study, a fluid-dynamic effect was observed during the chromatographic purification of an enveloped virus using a CEX monolith resin. This effect was found to be independent of virus batch, column scale and LC equipment. Standard mechanistic modeling approaches were used to understand the effect, but the models could not accurately represent the observed effect, leading to misalignment. Potential contributing factors were examined and discussed.

The convective entrapment effect was identified as plausible factor. This fluid-dynamic effect results in a retention of large biomolecules dependent on the convective flow and the biomolecules diffusional parameters. To the best of our knowledge, the entrapment was not yet simulated in a chromatographic model. Thus, we extended the SMA isotherm by a Langmuir term to include the retention of bioparticles resulted from convective entrapment. It was shown that the introduced approach with the combined isotherm was capable of representing tailing effects and consequently separation of population due to different convective entrapment behaviors. This allowed to investigate the effect in silico without an analytical panel which is not yet available. However, the presented isotherm approximates the entrapment and neglects dependencies e.g. flow rate, particle diffusion rate, resin channel geometries and concentration dependencies. Together with the simplification inherent in the Langmuir equation, some misalignments are still observed. The model application must be considered limited.

The observed convective entrapment effect has implications for both, preparative runs and analytical methods using resins with convective channels and large biomolecules. Polymerization processes of monoliths are intended to keep channel sizes constant across scales [63]. It is expected that scaled-up columns should behave like the scaled-down columns, and this was shown for lab scale columns. Tailing effects are to be expected across all scales at characteristic flow rates. Recovery losses due to entrapment should be evaluated, and CIP steps adjusted accordingly (e.g. low flow rate steps or flow rate pauses during CIP phases can be incorporated). For analytical applications, the impact of entrapment may be more significant due to shifted retention times and tailings. Flow rate effects should be investigated and considered during method development. The separation of populations which was shown might be exploited for analytical purposes. More orthogonal analytical methods are necessary to understand the biophysical correlates leading to this separation.

In this study, the relevance to consider the entrapment effect was demonstrated. Although the proposed modeling approach was able to describe this effect, further studies and suitable analytical methods are necessary to gain more knowledge about this effect and its consequences.

Data availability

All data used to evaluate the conclusions of the article are present in the paper and/or supplementary material. ViraTherapeutics GmbH is unable to provide raw data, protocols or additional datasets.

CRediT authorship contribution statement

Adrian Schimek: Writing – original draft, Methodology, Investigation, Data curation, Conceptualization. **Judy Ng:** Writing – review & editing, Conceptualization. **Federico Will:** Writing – review & editing, Data curation. **Jürgen Hubbuch:** Writing – review & editing, Supervision.

Declaration of competing interest

The authors declare the following financial interests/personal relationships which may be considered as potential competing interests:

Adrian Schimek reports equipment, drugs, or supplies was provided by Sartorius BIA Separations doo. Adrian Schimek reports equipment, drugs, or supplies was provided by Cytiva Europe GmbH. Adrian Schimek and Judy Ng report a relationship with ViraTherapeutics GmbH that includes: employment. Federico Will reports a relationship with Boehringer Ingelheim Pharma GmbH & Co KG that includes: employment. Judy Ng has patent #US20220010286A1 pending to Boehringer Ingelheim International GmbH. If there are other authors, they declare that they have no known competing financial interests or personal relationships that could have appeared to influence the work reported in this paper.

Supplementary materials

Supplementary material associated with this article can be found, in the online version, at doi:10.1016/j.chroma.2025.465832.

References

[1] C.E. Dunbar, K.A. High, J.K. Joung, D.B. Kohn, K. Ozawa, M. Sadelain, Gene therapy comes of age, Science 359 (2018), https://doi.org/10.1126/science. aan4672.

[2] Q. Lan, S. Xia, Q. Wang, W. Xu, H. Huang, S. Jiang, L. Lu, Development of oncolytic virotherapy: from genetic modification to combination therapy, Front. Med. 14 (2020) 160–184, https://doi.org/10.1007/s11684-020-0750-4.

[3] Q. Ji, Y. Wu, A. Albers, M. Fang, X. Qian, Strategies for advanced oncolytic virotherapy: current technology innovations and clinical approaches, Pharmaceutics. 14 (2022) 1811, https://doi.org/10.3390/pharmaceutics14091811.

[4] A. Srivastava, K.M.G. Mallela, N. Deorkar, G. Brophy, Manufacturing challenges and rational formulation development for AAV viral vectors, J. Pharm. Sci. 110 (2021) 2609–2624, https://doi.org/10.1016/j.xphs.2021.03.024.

[5] N. Singh, C.L. Heldt, Challenges in downstream purification of gene therapy viral vectors, Curr. Opin. Chem. Eng. 35 (2022) 100780, https://doi.org/10.1016/j.coche.2021.100780.

[6] G.-A. Junter, L. Lebrun, Polysaccharide-based chromatographic adsorbents for virus purification and viral clearance, J. Pharm. Anal. 10 (2020) 291–312, https://doi.org/10.1016/j.jpha.2020.01.002.

[7] R. Kilgore, A. Minzoni, S. Shastry, W. Smith, E. Barbieri, Y. Wu, J.P. LeBarre, W. Chu, J. O'Brien, S. Menegatti, The downstream bioprocess toolbox for therapeutic viral vectors, J. Chromatogr. A (2023) 464337, https://doi.org/10.1016/j.chroma.2023.464337.

[8] B. Lins-Austin, S. Patel, M. Mietzsch, D. Brooke, A. Bennett, B. Venkatakrishnan, K. V. Vliet, A.N. Smith, J.R. Long, R. McKenna, M. Potter, B. Byrne, S.L. Boye, B. Bothner, R. Heilbronn, M. Agbandje-McKenna, Adeno-associated virus (AAV) capsid stability and liposome remodeling during endo/lysosomal pH trafficking, Viruses. 12 (2020) 668, https://doi.org/10.3390/v12060668.

[9] M. Rieser, J. Koch, G. Faccioli, K. Richter, T. Menzen, M. Biel, G. Winter, S. Michalakis, Comparison of different liquid chromatography-based purification strategies for adeno-associated virus vectors, Pharm 13 (2021) 748, https://doi.org/10.3390/pharmaceutics13050748.

[10] J. Turnbull, B. Wright, N.K. Green, R. Tarrant, I. Roberts, O. Hardick, D. G. Bracewell, Adenovirus 5 recovery using nanofiber ion-exchange adsorbents, Biotechnol. Bioeng. 116 (2019) 1698–1709, https://doi.org/10.1002/bit.26972.

[11] M. Krajacic, M. Ravnikar, A. Štrancar, I. Gutiérrez-Aguirre, Application of monolithic chromatographic supports in virus research, Electrophoresis 38 (2017) 2827–2836, https://doi.org/10.1002/elps.201700152.

[12] T. Vicente, M.F.Q. Sousa, C. Peixoto, J.P.B. Mota, P.M. Alves, M.J.T. Carrondo, Anion-exchange membrane chromatography for purification of rotavirus-like particles, J. Membrane Sci. 311 (2008) 270–283, https://doi.org/10.1016/j.memsci.2007.12.021.

[13] R. Hahn, A. Tscheliessnig, P. Bauerhansl, A. Jungbauer, Dispersion effects in preparative polymethacrylate monoliths operated in radial-flow columns, J. Biochem. Bioph. Meth. 70 (2007) 87–94, https://doi.org/10.1016/j.jbbm.2006.09.005.

[14] A. Jungbauer, R. Hahn, Polymethacrylate monoliths for preparative and industrial separation of biomolecular assemblies, J. Chromatogr. A 1184 (2008) 62–79, https://doi.org/10.1016/j.chroma.2007.12.087.

[15] F.C. Leinweber, U. Tallarek, Chromatographic performance of monolithic and particulate stationary phases hydrodynamics and adsorption capacity, J. Chromatogr. A 1006 (2003) 207–228, https://doi.org/10.1016/s0021-9673(03)00391-1.

[16] P. Nestola, R.J.S. Silva, C. Peixoto, P.M. Alves, M.J.T. Carrondo, J.P.B. Mota, Robust design of adenovirus purification by two-column, simulated moving-bed, size-exclusion chromatography, J. Biotechnol. 213 (2015) 109–119, https://doi.org/10.1016/j.jbiotec.2015.01.030.

[17] C.L. Effio, T. Hahn, J. Seiler, S.A. Oelmeier, I. Asen, C. Silberer, L. Villain, J. Hubbuch, Modeling and simulation of anion-exchange membrane chromatography for purification of Sf9 insect cell-derived virus-like particles, J. Chromatogr. A 1429 (2016) 142–154, https://doi.org/10.1016/j.chroma.2015.12.006.

[18] J.P. Mendes, M. Bergman, A. Solbrand, C. Peixoto, M.J.T. Carrondo, R.J.S. Silva, Continuous affinity purification of adeno-associated virus using periodic counter-current chromatography, Pharm 14 (2022) 1346, https://doi.org/10.3390/pharmaceutics14071346.

[19] W.R. Keller, A. Picciano, K. Wilson, J. Xu, H. Khasa, M. Wendeler, Rational downstream development for adeno-associated virus full/empty capsid separation – a streamlined methodology based on high-throughput screening and mechanistic modeling, J. Chromatogr. A 1716 (2024) 464632, https://doi.org/10.1016/j.chroma.2024.464632.

[20] S.M. Pirrung, L.A.M. van der Wielen, R.F.W.C. van Beckhoven, E.J.A.X. van de Sandt, M.H.M. Eppink, M. Ottens, Optimization of biopharmaceutical downstream processes supported by mechanistic models and artificial neural networks, Biotechnol. Prog. 33 (2017) 696–707, https://doi.org/10.1002/btpr.2435.

[21] J.M. Mollerup, T.B. Hansen, S. Kidal, L. Sejergaard, A. Staby, Development, modelling, optimisation and scale-up of chromatographic purification of a therapeutic protein, Fluid Phase Equilib. 261 (2007) 133–139, https://doi.org/10.1016/j.fluid.2007.07.047.

[22] G. Wang, T. Briskot, T. Hahn, P. Baumann, J. Hubbuch, Root cause investigation of deviations in protein chromatography based on mechanistic models and artificial neural networks, J. Chromatogr. A 1515 (2017) 146–153, https://doi.org/10.1016/j.chroma.2017.07.089.

[23] E.J. Close, J.R. Salm, D.G. Bracewell, E. Sorensen, A model based approach for identifying robust operating conditions for industrial chromatography with process variability, Chem. Eng. Sci. 116 (2014) 284–295, https://doi.org/10.1016/j.ces.2014.03.010.

[24] G. Pamenter, L. Davies, C. Knevelman, J. Miskin, K. Mitrophanous, D. Dikicioglu, D.G. Bracewell, Time-dependent sorption behavior of lentiviral vectors during anion-exchange chromatography, Biotechnol. Bioeng. (2023), https://doi.org/10.1002/bit.28483.

[25] T. Vicente, R. Fáber, P.M. Alves, M.J.T. Carrondo, J.P.B. Mota, Impact of ligand density on the optimization of ion-exchange membrane chromatography for viral vector purification, Biotechnol. Bioeng. 108 (2011) 1347–1359, https://doi.org/10.1002/bit.23058.

[26] H. Zhao, X. Lin, L. Wang, Y. Yang, H. Zhu, Z. Li, Z. Su, R. Yu, S. Zhang, Pore-blocking steric mass-action model for adsorption of bioparticles, J. Chromatogr. A 1726 (2024) 464968, https://doi.org/10.1016/j.chroma.2024.464968.

[27] A. Muik, I. Kneiske, M. Werbizki, D. Wilflingseder, T. Giroglou, O. Ebert, A. Kraft, U. Dietrich, G. Zimmer, S. Momma, D. von Laer, Pseudotyping vesicular Stomatitis virus with lymphocytic Choriomeningitis virus glycoproteins enhances infectivity for glioma cells and minimizes neurotropism, J. Virol. 85 (2011) 5679–5684, https://doi.org/10.1128/jvi.02511-10.

[28] P. Ge, J. Tsao, S. Schein, T.J. Green, M. Luo, Z. Hong Zhou, Cryo-EM model of the bullet-shaped Vesicular stomatitis virus, Science (1979) 327 (2010) 689–693, https://doi.org/10.1126/science.1181766.

[29] D. Mueller, A. Pardo Garcia, T.A. Grein, F. Kaess, J. Ng, K. Pesta, S. Schneider, J. Turnbull, Process for producing a purified rhabdovirus from cell mass, 2022.

[30] E.I. Trilisky, A.M. Lenhoff, Flow-dependent entrapment of large bioparticles in porous process media, Biotechnol. Bioeng. 104 (2009) 127–133, https://doi.org/10.1002/bit.22370.

[31] R. Hahn, M. Panzer, E. Hansen, J. Mollerup, A. Jungbauer, Mass transfer properties of monoliths, Separ Sci. Technol. 37 (2007) 1545–1565, https://doi.org/10.1081/ss-120002736.

[32] E.I. Trilisky, A.M. Lenhoff, Effect of bioparticle size on dispersion and retention in monolithic and perfusive beds, J. Chromatogr. A 1217 (2010) 7372–7384, https://doi.org/10.1016/j.chroma.2010.09.040.

[33] N. Pavlin, U. Černigoj, M. Bavčar, T. Plesničar, J. Mavri, M. Zidar, M. Bone, U. K. Savič, T. Sever, A. Štrancar, Analytical separation of plasmid DNA isoforms using anion exchanging chromatographic monoliths with 6 μm channels, Electrophoresis 44 (2023) 1967–1977, https://doi.org/10.1002/elps.202300031.

[34] Š. Kralj, Š.M. Kodermac, I. Bergoč, T. Kostelec, A. Podgornik, A. Štrancar, U. Černigoj, Effect of plasmid DNA isoforms on preparative anion exchange chromatography, Electrophoresis 44 (2023) 1953–1966, https://doi.org/10.1002/elps.202200035.

[35] B. Gabor, U. Černigoj, M. Barut, A. Štrancar, Reversible entrapment of plasmid deoxyribonucleic acid on different chromatographic supports, J. Chromatogr. A 1311 (2013) 106–114, https://doi.org/10.1016/j.chroma.2013.08.075.

[36] S. Golshan-Shirazi, G. Guiochon, Theoretical advancement in chromatography and related separation techniques. The Equilibrium-Dispersive Model of Chromatography, 1992, pp. 35–59, https://doi.org/10.1007/978-94-011-2686-1_2.

[37] G. Guiochon, D.G. Shirazi, A. Felinger, A.M. Katti, Fundamentals of preparative and nonlinear chromatography, 2006. doi:10.1016/b978-012370537-2/50034-5.

[38] P.V. Danckwerts, Continuous flow systems distribution of residence times, Chem. Eng. Sci. 2 (1953) 1–13, https://doi.org/10.1016/0009-2509(53)80001-1.

[39] C.A. Brooks, S.M. Cramer, Steric mass-action ion exchange: displacement profiles and induced salt gradients, AIChE J. 38 (1992) 1969–1978, https://doi.org/10.1002/aic.690381212.

[40] T. Hahn, T. Huuk, A. Osberghaus, K. Doninger, S. Nath, S. Hepbildikler, V. Heuveline, J. Hubbuch, Calibration-free inverse modeling of ion-exchange chromatography in industrial antibody purification, Eng. Life Sci. 16 (2015) 107–113, https://doi.org/10.1002/elsc.201400248.

[41] J. Diedrich, W. Heymann, S. Leweke, S. Hunt, R. Todd, C. Kunert, W. Johnson, E. von Lieres, Multi-state steric mass action model and case study on complex high loading behavior of mAb on ion exchange tentacle resin, J. Chromatogr. A 1525 (2017) 60–70, https://doi.org/10.1016/j.chroma.2017.09.039.

[42] S. Wilmschen, S. Schneider, F. Peters, L. Bayer, L. Issmail, Z. Bánki, T. Grunwald, D. von Laer, J. Kimpel, RSV vaccine based on rhabdoviral vector protects after single immunization, Vaccines (Basel) 7 (2019) 59, https://doi.org/10.3390/vaccines7030059.

[43] G. Kärber, Beitrag zur kollektiven Behandlung pharmakologischer Reihenversuche, Naunyn-Schmiedebergs Arch. Für Exp. Pathol. Pharmakol 162 (1931) 480–483, https://doi.org/10.1007/bf01863914.

[44] C. Spearman, The method of "right and wrong cases" ('constant stimuli') without Gauss formulae, Br. J. Psychol. 2 (1908) 227–242, https://doi.org/10.1111/j.2044-8295.1908.tb00176.x, 19041920.

[45] A. Schimek, J.K.M. Ng, I. Basbas, F. Martin, D. Xin, D. Saleh, J. Hubbuch, An HPLC-SEC-based rapid quantification method for vesicular stomatitis virus particles to facilitate process development, Mol. Ther. - Methods Clin. Dev. (2024) 101252, https://doi.org/10.1016/j.omtm.2024.101252.

[46] S. Leweke, E. von Lieres, Chromatography analysis and Design toolkit (CADET), Comput. Chem. Eng. 113 (2018) 274–294, https://doi.org/10.1016/j.compchemeng.2018.02.025.

[47] J. Schmölder, M. Kaspereit, A modular framework for the modelling and optimization of advanced chromatographic processes, Processes 8 (2020) 65, https://doi.org/10.3390/pr8010065.

[48] S. Yamamoto, Plate height determination for gradient elution chromatography of proteins, Biotechnol. Bioeng. 48 (1995) 444–451, https://doi.org/10.1002/bit.260480506.

[49] J. Blank, K. Deb, Pymoo: multi-objective optimization in Python, IEEe Access. 8 (2020) 89497–89509, https://doi.org/10.1109/access.2020.2990567.

[50] T.C. Huuk, T. Briskot, T. Hahn, J. Hubbuch, A versatile noninvasive method for adsorber quantification in batch and column chromatography based on the ionic capacity, Biotechnol. Prog. 32 (2016) 666–677, https://doi.org/10.1002/btpr.2228.

[51] T. Ishihara, T. Kadoya, H. Yoshida, T. Tamada, S. Yamamoto, Rational methods for predicting human monoclonal antibodies retention in protein A affinity chromatography and cation exchange chromatography structure-based chromatography design for monoclonal antibodies, J. Chromatogr. A 1093 (2005) 126–138, https://doi.org/10.1016/j.chroma.2005.07.077.

[52] J.J. van Deemter, F.J. Zuiderweg, A. Klinkenberg, Longitudinal diffusion and resistance to mass transfer as causes of nonideality in chromatography, Chem. Eng. Sci. 5 (1956) 271–289, https://doi.org/10.1016/0009-2509(56)80003-1.

[53] G. Desmet, K. Broeckhoven, Extra-column band broadening effects in contemporary liquid chromatography: causes and solutions, TrAC Trends Anal. Chem. 119 (2019) 115619, https://doi.org/10.1016/j.trac.2019.115619.

[54] S. Yamamoto, T. Okada, M. Abe, N. Yoshimoto, Peak spreading in linear gradient elution chromatography with a thin monolithic disk, J. Chromatogr. A 1218 (2011) 2460–2466, https://doi.org/10.1016/j.chroma.2011.03.013.

[55] T. Fornstedt, G. Zhong, G. Guiochon, Peak tailing and slow mass transfer kinetics in nonlinear chromatography, J. Chromatogr. A 742 (1996) 55–68, https://doi.org/10.1016/0021-9673(96)00323-8.

[56] S.H. Altern, J.P. Welsh, J.Y. Lyall, A.J. Kocot, S. Burgess, V. Kumar, C. Williams, A. M. Lenhoff, S.M. Cramer, Isotherm model discrimination for multimodal chromatography using mechanistic models derived from high-throughput batch isotherm data, J. Chromatogr. A 1693 (2023) 463878, https://doi.org/10.1016/j.chroma.2023.463878.

[57] D. Xin, L. Kurien, K. Briggs, A. Schimek, R. Dambra, D. Hochdorfer, T.A. Arnouk, M. Brgles, S. Gautam, D. Hotter, J. Solzin, T. Kriehuber, J. Ashour, A. Vigil, M. Hawley, X. He, Characterization of VSV-GP morphology by CryoEM imaging and SEC-MALS, Mol. Ther. Methods Clin. Dev. (2025) 101429, https://doi.org/10.1016/j.omtm.2025.101429.

[58] M. de las M. Segura, A. Kamen, P. Trudel, A. Garnier, A novel purification strategy for retrovirus gene therapy vectors using heparin affinity chromatography, Biotechnol. Bioeng. 90 (2005) 391–404, https://doi.org/10.1002/bit.20301.

[59] D. Sviben, D. Forčić, T. Kurtović, B. Halassy, M. Brgles, Stability, biophysical properties and effect of ultracentrifugation and diafiltration on measles virus and mumps virus, Arch. Virol. 161 (2016) 1455–1467, https://doi.org/10.1007/s00705-016-2801-3.

[60] H. Koku, R.S. Maier, M.R. Schure, A.M. Lenhoff, Modeling of dispersion in a polymeric chromatographic monolith, J. Chromatogr. A 1237 (2012) 55–63, https://doi.org/10.1016/j.chroma.2012.03.005.

[61] H.F. Lodish, M. Porter, Heterogeneity of vesicular stomatitis virus particles: implications for virion assembly, J. Virol. 33 (1980) 52–58, https://doi.org/10.1128/jvi.33.1.52-58.1980.

[62] I. Mihelič, D. Nemec, A. Podgornik, T. Koloini, Pressure drop in CIM disk monolithic columns, J. Chromatogr. A 1065 (2005) 59–67, https://doi.org/10.1016/j.chroma.2004.10.054.

[63] A. Podgornik, M. Barut, A. Štrancar, D. Josić, T. Koloini, Construction of large-volume monolithic columns, Anal. Chem. 72 (2000) 5693–5699, https://doi.org/10.1021/ac000680o.